Computational Materials Science 147 (2018) 132–136

Contents lists available at ScienceDirect

Computational Materials Science

journal homepage: www.elsevier.com/locate/commatsci

Phonon thermal transport in monolayer FeB_2 from first principles

Xiuxian Yang [a], Zhenhong Dai [a,*], Yinchang Zhao [a], Sheng Meng [b,c]

[a] Department of Physics, Yantai University, Yantai 264005, People's Republic of China
[b] Beijing National Laboratory for Condensed Matter Physics and Institute of Physics, Chinese Academy of Sciences, Beijing 100190, People's Republic of China
[c] Collaborative Innovation Center of Quantum Matter, Beijing 100084, People's Republic of China

ARTICLE INFO

Article history:
Received 7 December 2017
Received in revised form 23 January 2018
Accepted 25 January 2018
Available online 9 February 2018

Keywords:
Thermal transport
Two dimensional material
Thermoelectric properties
Boron-based Dirac material

ABSTRACT

We investigate the phonon thermal transport in two-dimensional (2D) metal-boride material (FeB_2) by combining the phonon Boltzmann transport equation with first principle calculations. Strikingly, a fairly low lattice thermal conductivity, such as 51.9 W/mK at room temperature, is discovered in this new 2D monolayer boron-based Dirac material. Our analyses indicate that the low lattice thermal conductivity is resulted from the strong three-phonon scattering and the low phonon group velocity. Due to relatively weak three-phonon scattering, the out-of-plane acoustic phonon modes play a significant role in the thermal transport of this monolayer FeB_2. In addition, we also study the size dependence of thermal conductivity for applications in design of nanometer devices.

1. Introduction

Due to novel electronic and thermal properties, two-dimensional (2D) materials have attracted great interests in the last decades [1–4]. A great many of 2D materials such as graphene [5], silicene [6,7], graphynes [8], and boron monolayer [9–11], etc. have been investigated theoretically and experimentally to an extensive extent. As a neighbour of carbon in the periodic table of chemical element, boron has been expected to have similar properties to carbon, which thus stimulates a great interest in the search of boron monolayers and boron-based 2D materials [12,13]. Hence, the structural and electronic properties of boron monolayers and boron-based 2D materials have been also studied extensively [9]. Most recently, the triangular boron monolayer and the monolayers with hexagonal lattice as vacancies were successfully synthesized in laboratory through growth on a silver surface under pristine ultrahigh vacuum conditions [10,11]. This successful fabrication arouses more enthusiasm in the research of the properties of boron monolayers. Interestingly, it is found that borophene has much low thermal conductivity compared with graphene. For example, the lattice thermal conductivity of borophene is reported to be only 2.4% of that of graphene [14]. At the same time, enlightened by the boron monolayers, a great many of boron-based 2D materials have been also extensively studied.

To date, many boron-based 2D materials have been reported, such as 2D FeB_6 [15], MgB_6 [16] crystal, lithium-boron (Li-B) monolayers [17], the planar CoB_{18} [18], and the monolayer FeB_2 [19]. In these materials, the sTable 2D FeB_2 possesses a unique property with a Dirac state around the fermi level [19]. Thus it is a good candidate for the design of Dirac material in theory. Anatomically, 2D FeB_2 can be taken as a monolayer formed by honeycomb boron network with Fe atom inserted in the center of the honeycomb. Moreover, Fe atom provides electron to B network, which accounts for the structural stability of this monolayer configuration [19]. Generally, the materials containing heavy elements, such as $IrSb_3$ [20], *n*-type TiO_2 polymorphs [21], CdO [22] and $PbTiO_3$ [23], etc., have low phonon frequency, low group velocities, and strong phonon scatterings, which usually leads to a low thermal conductivity. Enlightened by this, we expect that FeB_2 possesses a low thermal conductivity due to the presence of heavy element Fe. In this paper, we calculate the lattice thermal conductivity κ_L of monolayer FeB_2, which represents the total thermal conductivity in this monolayer due to the presence of Dirac state at the Fermi level. Strikingly, a fairly low lattice thermal conductivity, such as 51.9 W/mK at room temperature, is discovered in this material. We show that this low lattice thermal conductivity is resulted from the strong three-phonon scattering and low phonon group velocity. In addition, we also studied the size dependence of thermal conductivity for applications in design of nanometer devices. The paper is organized as follows: In Section 2, we briefly discuss the theoretical methods. In Section 3, the results of thermal conductivity and the discussion of factors dominating thermal transport are presented. Section 4 provides the our summary.

* Corresponding author.
E-mail addresses: zhdai@ytu.edu.cn (Z. Dai), smeng@iphy.ac.cn (S. Meng).

https://doi.org/10.1016/j.commatsci.2018.01.050
0927-0256/

2. Methodology

To obtain accurate thermal transport properties, we calculate the lattice thermal conductivity κ_L by using phonon Boltzmann transport equation (BTE) combined with the interatomic force constants (IFCs) obtained from the first-principles density functional theory (DFT) calculations [24]. The lattice thermal conductivity κ_L along the α direction can be written as

$$\kappa_L^{\alpha\alpha} = \frac{1}{k_B T^2 \Omega N} \sum_{\mathbf{q},\upsilon} f_0(f_0+1)(\hbar\omega_{\mathbf{q},\upsilon}) v_g^{\alpha,\mathbf{q},\upsilon} F_{\mathbf{q},\upsilon}^{\alpha}, \quad (1)$$

where $\mathbf{q}$ is wave vector and υ is phonon branch, κ_B is Boltzmann constant, Ω is the unit cell volume, N is the number of quasi continuous q points uniformly sampled in the first Brillouin zone (BZ), and f_0 is the equilibrium Bose-Einstein distribution function. $\hbar$ is the reduced Planck constant, $\omega_{\mathbf{q},\upsilon}$ is the phonon frequency of the υth phonon mode, and $v_g^{\alpha,\mathbf{q},\upsilon}$ represents the phonon group velocity of υth mode along the α direction. Due to the scattering source is the two- and three-phonon process, $F_{\mathbf{q},\upsilon}^{\alpha}$ is determined by the formula [25]

$$F_{\mathbf{q},\upsilon}^{\alpha} = \tau_{\mathbf{q},\upsilon}(v_g^{\alpha,\mathbf{q},\upsilon} + \Delta_{\mathbf{q},\upsilon}) \quad (2)$$

where $\tau_{\mathbf{q},\upsilon}$ is the phonon lifetime in relaxation time approximation (RTA). $\Delta_{\mathbf{q},\upsilon}$ is a correction term used to eliminate the inaccuracy of RTA via solving the BTE iteratively. If $\Delta_{\mathbf{q},\upsilon}$ is ignored, the $\kappa_L^{\alpha\alpha}$ in RTA is obtained. The ShengBTE package is employed to calculate the κ_L [26]. The acquired harmonic and anharmonic interatomic force constants (IFCs) are generated within the $5 \times 5 \times 1$ supercells by the finite-difference approach, which are calculated based on the density functional theory (DFT) software package VASP [27] through the Phonopy program [28] for harmonic IFCs and THIRDORDER.PY script [26] for anharmonic IFCs. In the calculations of anharmonic IFCs, the interaction up to the fourth nearest neighbors is included. In DFT calculations, the projector augmented wave potentials (PAW) is used to simulate the ion core, and the valance electron is modeled by a plan-wave basis sets with the cutoff energy of 500 eV and the generalized gradient approximation (GGA) of the Perdew-Burke-Ernzerhof (PBE) [29]. A vacuum spacing of 15 Å is applied to avoid the interactions between the adjoining imaginary layers. For relaxation of primitive cell, the force acting on each atom is less than 10^{-4} eV/Å, the electronic stopping criterion is set to be 10^{-8} eV, and a $15 \times 15 \times 15$ Γ-centered Monkhorst-Pack k-point grid is used to simulate the Brillouin zone summation. For calculations of the supercells, to ensure the same density of k-point sampling with that of the primitive cell, the $3 \times 3 \times 1$ k-mesh is used. Finally, a $30 \times 30 \times 1$ q-mesh is selected to sample the corresponding phonon wave-vector mesh for the ShengBTE calculations. Due to the presence of magnetic atom Fe, it is necessary to consider the influence of spin polarization on the energy band structure and κ_L. However, through our calculations, we find that the results of the two method (spin polarization or non-spin polarization) are nearly the same.

3. Results and discussion

The optimized structure of monolayer FeB_2 is shown in Fig. 1(a). It is composed of a plane boron configuration similar to graphene but with a Fe atom inserted in the center of the boron hexagonal lattice. In this monolayer sheet, each Fe atom coordinates with six boron atoms around it, and thus forms planar hexacoordination. The optimized B-B and Fe-B bond lengths are 1.82 Å and 1.93 Å, respectively, and the inserted Fe atom deviates about 0.59 Å from the graphene-like boron layer, which leads to a low-buckled configuration of the monolayer FeB_2, as shown in the lateral view of Fig. 1(a). These structural parameters are in good agreement with the previous work which gives the B-B bond length, Fe-B bond length, and buckling of 1.83 Å, 1.93 Å, and 0.60 Å, respectively [19].

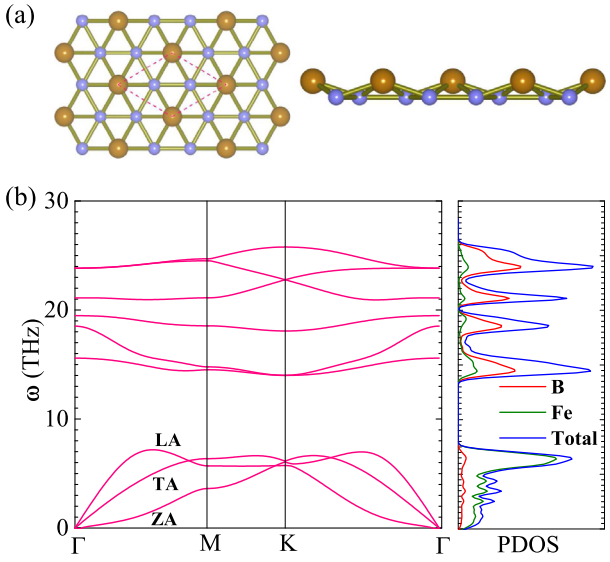

Fig. 1. (a) Top and lateral view of monolayer FeB_2. The big and small balls represent the Fe and B atoms, respectively. (b) Phonon dispersion and phonon density of states (PDOS) of monolayer FeB_2. The acoustic phonon modes and optical phonon modes are divided by a gap of about 6.68 THz. The three acoustic modes are marked with ZA, TA, and LA according to their vibrational characters.

The phonon dispersion spectrum and the phonon density of states (PDOS) with the partial PDOS of Fe and B atoms are shown in Fig. 1(b). Because of the existence of three atoms in each primitive cell, there are 9 phonon branches. According to the vibrational characters, the three acoustic branches are named as the out-of-plane acoustic (ZA), transverse acoustic (TA), and longitudinal acoustic (LA) phonon modes, respectively. The flexural ZA acoustic branch is the softest vibration mode, which corresponds to the out-of-plane transverse motion or bending of the FeB_2 sheet, and possesses an approximate parabolic dispersion feature around the Γ point. Between the acoustic and the optical branches, there is a gap of about 6.68 THz, which is similar to the highest acoustic phonon frequency. The partial PDOS shows that low frequency are governed mainly by Fe atoms while B atoms dominate the vibrations of high frequency, which is due to the heavier mass of Fe than that of B.

The calculated intrinsic lattice thermal conductivity κ_L of the naturally occurring monolayer FeB_2 is plotted in Fig. 2. According to Eq. (1), the original κ_L obtained from the BTE calculations should be re-scaled by a factor of c/h, where c is the lattice constant along the normal direction and h is the effective thickness of the monolayer FeB_2 sheet. In our calculations, c is fixed at the vacuum spacing of 15.00 Å. To obtain a precise h, we optimize the bilayer FeB_2, just like MXenes [30]. The calculated h is 2.575 Å which is the distance between two boron atom layers equivalent in the corresponding monolayer FeB_2. The DFT-D2 method is adopted since the van der Waals (VDW) is remarkably for layer interactions. The iterative solutions (ITS) and the RTA results are both shown in Fig. 2. Overall, the κ_L decreases as the increase of the temperature T. At 300 K, the re-scaled κ_L obtained from ITS and RTA are 51.9 W/mK and 28.4 W/mK, respectively. At high temperature (1000 K), the ab initio molecular dynamics simulations confirms that the FeB_2 sheet can maintain its original configuration with hexacoordinated Fe atoms and graphene-like arranged boron sheet [19]. Compared with other 2D materials, the calculated κ_L of the

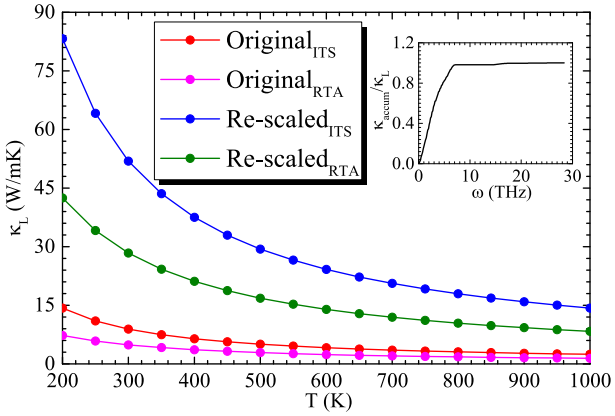

Fig. 2. Calculated lattice thermal conductivity κ_L of monolayer FeB_2 sheet as a function of temperature T ranging from 200 K to 1000 K. The inset shows the scaled cumulative thermal conductivity versus the allowed phonon frequency at 300 K.

monolayer FeB_2 sheet at 300 K is smaller than those of blue phosphorene ($\kappa_L \sim 78$ W/mK) [31], and graphene ($\kappa_L \sim 3000$ W/mK) [32]. In addition, the cumulative thermal conductivity versus the allowed phonon frequency reveals that the κ_L of the monolayer FeB_2 is mainly dominated by the phonons with the frequency below 7 THz, which are just right the acoustic phonons, as shown in the inset of Fig. 2.

To investigate the size dependence of the lattice thermal transport, we also calculate the cumulative thermal conductivity with respect to the allowed phonon maximum mean-free path (MFP) at 300 K, as shown in Fig. 3(a). The cumulated κ_L keeps increasing as the MFP increases, until achieving the thermodynamic limit L_{diff} [33], which represents the heat carriers for the longest phonon MFP and possesses a value of 265.05 nm for the monolayer FeB_2.

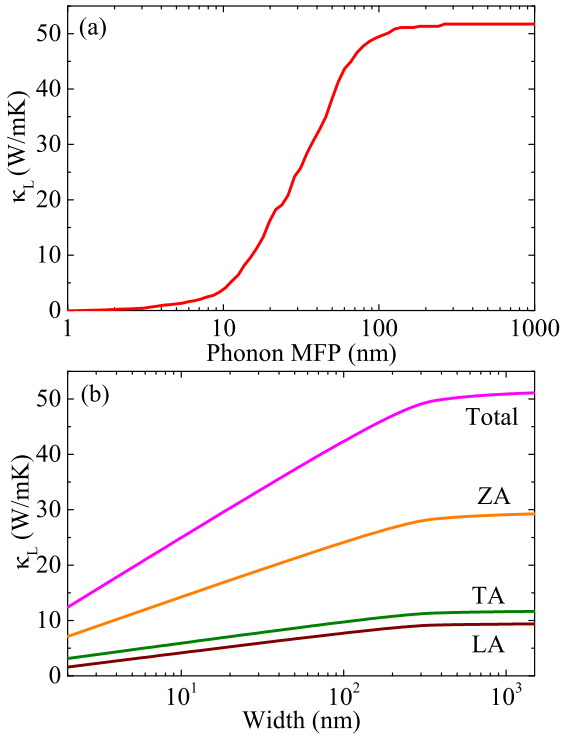

Fig. 3. (a) Cumulative thermal conductivity of monolayer FeB_2 sheet as a function of allowed phonon maximum mean-free path (MFP) at 300 K. (b) Thermal conductivity of the FeB_2 nanowires as a function of the width at 300 K.

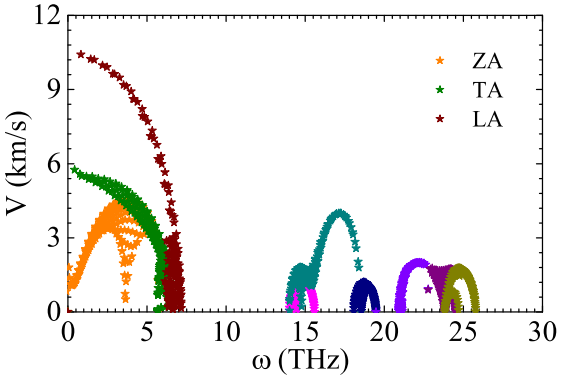

Fig. 4. Phonon group velocities within the first Brillouin zone (BZ).

Furthermore, phonons with MFPs smaller than 50 nm devote about 75% of the total κ_L. This signifies that the nanostructuring with the length of 50 nm would reduce the κ_L by 25%. That is, to reduce the κ_L of monolayer FeB_2 significantly, nanostructures with characteristic length smaller than 50 nm is required. In Fig. 3(b), we plot the thermal conductivity of the FeB_2 nanowires as a function of the width at 300 K. It exhibits that a nanowire with the width of 50 nm has a $\kappa_L \sim 37.1$ W/mK, which is about 79% of the total κ_L, and consistent with the result obtained from the analyses of cumulated κ_L versus the allowed phonon MFP. From Fig. 3(b), one can also find that the κ_L is mainly devoted by three acoustic branches. The ZA branch possesses the largest contribution to the κ_L, which takes up about 57% of the total κ_L, and the TA and LA branches occupy about 23% and 18% of the total κ_L, respectively.

On the other side, we also calculated the group velocities of each phonon mode shown in the phonon spectrum. The phonon group velocities as a function of frequency within the first Brillouin zone (BZ) are shown in Fig. 4. The origin, green and wine stars represent the ZA, LA, TA modes, respectively, and other colors represent different optic modes. Due to less contributions of optic modes, we did not mark them in the figure. At the low frequency, the group velocities at the long-wavelength limit are about 10.43 km/s, 5.78 km/s, 1.80 km/s for LA, TA, ZA, respectively. The group velocities of FeB_2 are compared to 5400–8800 m/s in silicene [34], 4000–8000 m/s in the blue phosphorene [35], and 3700–6000 m/s in the graphene [36]. In our expectation, because the low frequency acoustic phonons lead to the majority phonon transport, moreover within the optic spectrum some high frequency modes are not contributing. The group velocities of ZA branch is smaller than the LA branch, TA branch, at the frequency range 0–6.4 THz, as shown in Fig. 4. Therefore, our results indicated that the ZA branch play a important role in the thermal transport.

The mode (γ_j) Grüneisen parameter often provides the anharmonic interactions information, and is given by

$$\gamma_j(\vec{q}) = -\frac{a_0}{\omega_j(\vec{q})}\frac{\partial \vec{q}}{\partial a} \tag{3}$$

where γ_j is the Grüneisen parameter, $\vec{q}$ is the wave vector, a_0 is the equilibrium lattice constant, j is phonon branch index, and ω is the frequency. The κ_L can use the heat capacity written the following form

$$\kappa = \frac{1}{3}C_v\tau\bar{v}^2 \tag{4}$$

where the C_v is the unit volume heat capacity, τ is the relaxation time, the $\bar{v}$ is the average velocity. As shown in Fig. 5(a), the thermal capacity C_V becomes larger as the temperature increases, finally the curve tends to be smooth. In Fig. 5(b), we calculated the Grüneisen

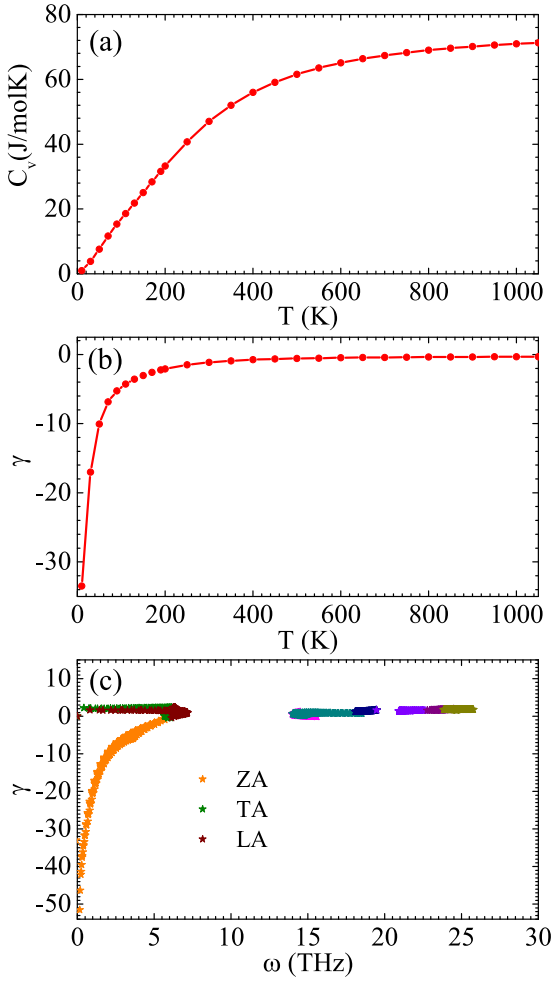

Fig. 5. (a) Constant volume heat capacity of temperature ranging from 0 K to 1000 K. (b) Calculated Grneisen parameters of temperature ranging from 0 K to 1000 K. (c) The calculated Grüneisen parameters within the first BZ at 300 K.

parameter γ, which is a negative number. As we all known, Grüneisen parameter can determine the thermal expansion and given by

$$\gamma = -\frac{dln\omega}{dlnV} \tag{5}$$

where the ω is frequency, V is the volume. Therefore, we found a magical phenomenon in FeB_2 that this new 2D material FeB_2 is contract when heated and expand when cooled, but it is beyond range of our discussion. In the first BZ, we found the optic branches, the TA branch and the LA branch at the Grüneisen parameters is equal to zero or so, which indicated these phonons are harmonic approximation, hence, these are almost not contribute to κ_L. However, the ZA phonon branch deviates from the Grüneisen parameters is extremely larger, therefore, the anharmonicity interaction is seemly dominated by the ZA phonon branch.

As can be seen from the above, the acoustic phonon modes contribute the most to the κ_l in FeB_2, and in other most 2D semiconductor or insulator materials usually have the same feature. In order to investigation the reasons for the acoustic modes or ZA phonon branch contribute most to κ_L, it is worthwhile to research the relaxation times or lifetimes of each phonon mode as the function of frequency. Because the size of phonon lifetimes or relaxation times reflect the strength of anharmonicity, the larger anharmonicity gives the smaller phonon lifetimes. The relationship between the thermal conductivity and the relaxation times is the Eq. (5). Therefore, the τ can affect the thermal conductivity, so

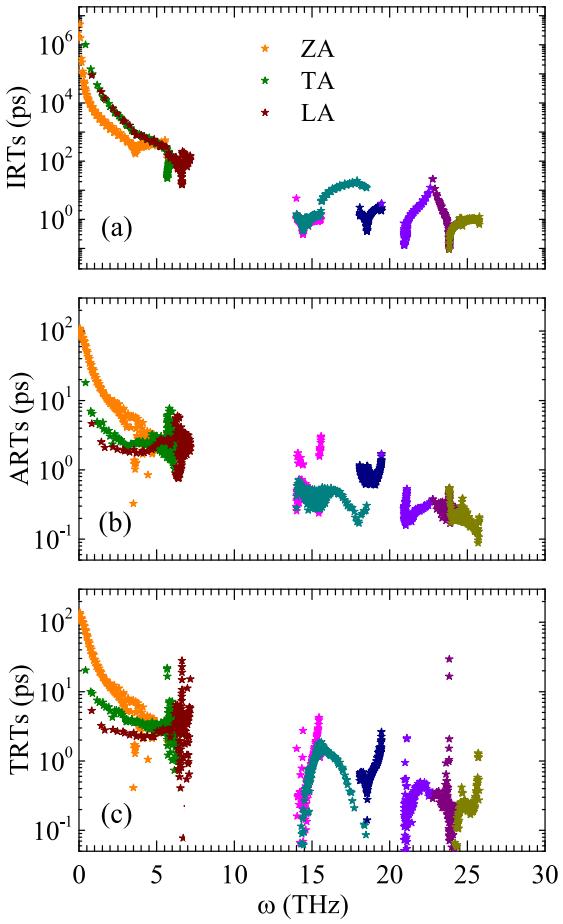

Fig. 6. The isotopic (a), anharmonic (b) and total (c) relaxation time of each phonon branch as a function of frequency.

we studied the relaxation times of FeB_2. As shown in Fig. 6(a)–(c), we calculate the isotopic relaxation times (IRTs), anharmonic relaxation times (ARTs) and total relaxation times (TRTs), respectively. The total relaxation time is a consists of contribution by the isotopic relaxation time and the anharmonic relaxation time

$$\frac{1}{\tau_j(\vec{q})} = \frac{1}{\tau_j(\vec{q})^{anh}} + \frac{1}{\tau_j(\vec{q})^{iso}} \tag{6}$$

the $\frac{1}{\tau}$ is the scattering rates. From Fig. 6(a) and (c), we discovered that the isotopic scattering process is weak compared to the anharmonic scattering process. In addition, the isotopic scattering process is affected by the abundance of isotopes of this element in nature and the isotopes of B are only 19% in nature [26,37]. From Fig. 6 (b) and (c), we found the anharmonic scattering process is strong, and the anharmonic scattering process corresponds to the three-phonon process. In Fig. 6(c), the anharmonic relaxation times of ZA mode contribute smallest to the total scattering rate, and according to the Eq. (5) we can know this relationship. Therefore, from Fig. 6 and Eq. (6), we observed the anharmonic relaxation time dominate the total relaxation time. Noticed that typically the available phase space vary inversely with the relaxation times and κ_L. As is well known, the $\tau_j(\vec{q})^{anh}$ is related to the anharmonic IFC3 and the weighted phase space of three-phonon process (WP3). Because the WP3 contains a large number of scattering events of satisfying the energy and momentum conservation conditions [38], we used WP3 to assess quantitatively the number of scattering channels for each phonon mode. The three-phonon processes in the phase

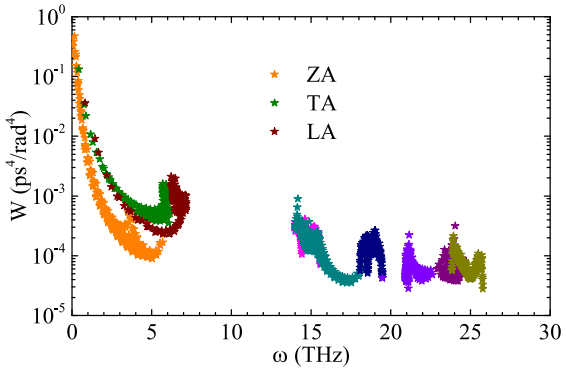

Fig. 7. The corresponding weighted phase space WP3.

space is unrestricted that indicates there are a lot of number of available scattering channels. Thus, between the intrinsic lattice thermal conductivity and the WP3, there is an inverse relationship [39].

As previous works has shown that among many simple systems, the WP3 is a powerful indicator of the κ_L [40]. To gain further investigation the mechanism of the phonon scattering, we calculated the WP3 as a function of frequency, and the result is shown in Fig. 7. The WP3 reflect the scattering rate, which is proportional to the reciprocal of the relaxation time. As shown in Fig. 7, at the low frequency range about 0–6.4 THz, the scattering rate of the ZA phonon branch is smaller than LA and TA phonon branches in the WP3. Therefore, we can know that the ZA phonon branch has smaller scattering rate, which dominates the phonon transport, and leads to a large κ_L. And Fig. 7 reveals in FeB_2 that the acoustic phonons scattering process dominates the phonon transport, and leads to a low lattice thermal conductivity κ_L. Moreover, the ZA phonon modes dominate the scattering process of all phonon modes.

4. Conclusion

In conclusion, we employed the phonon Boltzmann transport theory combined with the first-principles calculation to calculate the lattice thermal conductivity κ_L of the recently predicted the two-dimensional boron-based material FeB_2 which has a Dirac state in the fermi level. A fairly low lattice thermal conductivity (51.9 W/mK) is discovered in FeB_2. We find that this low lattice thermal conductivity is resulted from the heavier atoms (Fe), the low acoustic phonons group velocity, the low acoustic phonons frequency, the strong three-phonon scattering process and small phonon lifetimes. The phase space is an important tool to understand the lifetimes for the three-phonon scattering process and describes the trend of thermal transport in FeB_2. We find that the anharmonic process is much stronger in the FeB_2 and gives the strong thermal resistance. Moreover, the anharmonicity is also a feature of the Grüneisen parameter and the anharmonic effect is determined the κ_L in FeB_2. In three acoustic modes, the out-of-plane acoustic mode (ZA) play important roles in the thermal transport than others. In addition, we found a very interesting phenomenon, the new 2D material FeB_2 is a heat shrinkable and cold inflated material due to the Grüneisen parameter is a negative value. Our work is highlights the important role of the anharmonic process in determining the κ_L and the thermal transport properties in 2D Dirac boron-based materials.

Acknowledgment

This research were supported by the National Natural Science Foundation of China under Grant Nos. 11774396 and 11704322, Shandong Natural Science Funds for Doctoral Program under Grant No. ZR2017BA017, the National Key Research and Development Program of China under Grant No. 2016YFA0300902, and the MOST Project of China under Grant No. 2015CB921001.

References

[1] A.C. Ferrari, F. Bonaccorso, V. Fal'Ko, K.S. Novoselov, S. Roche, P. Bøggild, S. Borini, F.H. Koppens, V. Palermo, N. Pugno, et al., Nanoscale 7 (2015) 4598.
[2] J. Klinovaja, D. Loss, Phys. Rev. B 88 (2013) 075404.
[3] M. Zebarjadi, K. Esfarjani, M. Dresselhaus, Z. Ren, G. Chen, Energy Environ. Sci. 5 (2012) 5147.
[4] J.P. Heremans, V. Jovovic, E.S. Toberer, A. Saramat, K. Kurosaki, A. Charoenphakdee, S. Yamanaka, G.J. Snyder, Science 321 (2008) 554.
[5] A.H. Castro Neto, F. Guinea, N.M.R. Peres, K.S. Novoselov, A.K. Geim, Rev. Mod. Phys. 81 (2009) 109.
[6] S. Cahangirov, M. Topsakal, E. Aktürk, H. ahin, S. Ciraci, Phys. Rev. Lett. 102 (2009) 236804.
[7] H. Xie, M. Hu, H. Bao, Appl. Phys. Lett. 104 (2014) 131906.
[8] D. Malko, C. Neiss, F. Viñes, A. Görling, Phys. Rev. Lett. 108 (2012) 086804.
[9] X.-F. Zhou, X. Dong, A.R. Oganov, Q. Zhu, Y. Tian, H.-T. Wang, Phys. Rev. Lett. 112 (2014) 085502.
[10] A.J. Mannix, X.-F. Zhou, B. Kiraly, J.D. Wood, D. Alducin, B.D. Myers, X. Liu, B.L. Fisher, U. Santiago, J.R. Guest, M.J. Yacaman, A. Ponce, A.R. Oganov, M.C. Hersam, N.P. Guisinger, Science 350 (2015) 1513.
[11] B. Feng, J. Zhang, Q. Zhong, W. Li, S. Li, H. Li, P. Cheng, S. Meng, L. Chen, K. Wu, Nat. Chem. 8 (2016) 563.
[12] X. Zhang, Z. Zhang, X. Zhao, D. Wu, Z. Zhou, FlatChem 4 (2017) 42.
[13] Q. Tang, Z. Zhou, Z. Chen, Wiley Interdiscipl. Rev.: Comput. Mol. Sci. 5 (2015) 360.
[14] H. Sun, Q. Li, X. Wan, PCCP 18 (2016) 14927.
[15] J. Li, Y. Wei, X. Fan, H. Wang, Y. Song, G. Chen, Y. Liang, V. Wang, Y. Kawazoe, J. Mater. Chem. C 4 (2016) 9613.
[16] S.-Y. Xie, X.-B. Li, W.Q. Tian, N.-K. Chen, Y. Wang, S. Zhang, H.-B. Sun, PCCP 17 (2015) 1093.
[17] C. Wu, H. Wang, J. Zhang, G. Gou, B. Pan, J. Li, ACS Appl. Mater. Interfaces 8 (2016) 2526.
[18] W.-L. Li, T. Jian, X. Chen, T.-T. Chen, G.V. Lopez, J. Li, L.-S. Wang, Angew. Chem. 128 (2016) 7484.
[19] H. Zhang, Y. Li, J. Hou, A. Du, Z. Chen, Nano Lett. 16 (2016) 6124.
[20] W. Li, N. Mingo, Phys. Rev. B 90 (2014) 094302.
[21] D. Bayerl, E. Kioupakis, Phys. Rev. B 91 (2015) 165104.
[22] L. Lindsay, D.S. Parker, Phys. Rev. B 92 (2015) 144301.
[23] A. Roy, Phys. Rev. B 93 (2016) 100101.
[24] S. Baroni, S. De Gironcoli, A. Dal Corso, P. Giannozzi, Rev. Mod. Phys. 73 (2001) 515.
[25] W. Li, J. Carrete, N.A. Katcho, N. Mingo, Comput. Phys. Commun. 185 (2014) 1747.
[26] W. Li, J. Carrete, N.A. Katcho, N. Mingo, Comput. Phys. Commun. 185 (2014) 1747.
[27] G. Kresse, J. Furthmüller, Phys. Rev. B 54 (1996) 11169.
[28] A. Togo, F. Oba, I. Tanaka, Phys. Rev. B 78 (2008) 134106.
[29] J.P. Perdew, K. Burke, M. Ernzerhof, Phys. Rev. Lett. 77 (1996) 3865.
[30] X.-H. Zha, K. Luo, Q. Li, Q. Huang, J. He, X. Wen, S. Du, EPL (Europhys. Lett.) 111 (2015) 26007.
[31] A. Jain, A.J. McGaughey, Sci. Rep. 5 (2015) 8501.
[32] A.A. Balandin, S. Ghosh, W. Bao, I. Calizo, D. Teweldebrhan, F. Miao, C.N. Lau, Nano Lett. 8 (2008) 902, pMID: 18284217.
[33] A.C. Neto, F. Guinea, N.M. Peres, K.S. Novoselov, A.K. Geim, Rev. Modern Phys. 81 (2009) 109.
[34] X. Li, J.T. Mullen, Z. Jin, K.M. Borysenko, M.B. Nardelli, K.W. Kim, Phys. Rev. B 87 (2013) 115418.
[35] Z.-Y. Ong, E. Pop, Phys. Rev. B 84 (2011) 075471.
[36] T.-H. Liu, C.-C. Chang, Nanoscale 7 (2015) 10648.
[37] J. Meija, T.B. Coplen, M. Berglund, W.A. Brand, P.D. Bivre, M. Groning, N.E. Holden, J. Irrgeher, R.D. Loss, T. Walczyk, T. Prohaska, Pure Appl. Chem. (2016).
[38] B. Peng, H. Zhang, H. Shao, Y. Xu, X. Zhang, H. Zhu, Sci. Rep. 6 (2016).
[39] L. Lindsay, D. Broido, J. Phys.: Condens. Matter 20 (2008) 165209.
[40] T. Tadano, Y. Gohda, S. Tsuneyuki, Phys. Rev. Lett. 114 (2015) 095501.